Decoupling Reynolds Number and Reduced Velocity Effects in Characterization of Flow Induced Vibration of Rectangular Cylinders

Ross Cruikshank, David A. Olson, Ahmed M. Naguib
Department of Mechanical Engineering
Michigan State University
East Lansing, MI, 48824, USA
naguib@egr.msu.edu

ABSTRACT

Flow-induced vibration (FIV) of bluff bodies is commonly characterized using amplitude–reduced-velocity $\hat{y}^* - U_r$ plots, where U_r is varied by changing the freestream velocity approaching a freely oscillating body. This traditional method inevitably couples variations in Reynolds number with changes in reduced velocity, thereby obscuring the independent influence of Reynolds number on the underlying FIV mechanisms. In the present study, this ambiguity is resolved using an energy-map (EM) framework based on forced-oscillation experiments, which enables systematic decoupling of Reynolds number and U_r effects. Energy maps are obtained for large-aspect-ratio sharp- and round-corner rectangular cylinders undergoing transverse y oscillation in the Reynolds number range $800 \leq Re_d \leq 9500$ (based on cylinder thickness).

By coupling the energy maps with a prescribed oscillator cylinder model, $\hat{y}_c^* - U_r$ responses are reconstructed for different mass–damping parameters while holding Re_d fixed. For round-corner cylinders, the results demonstrate a pronounced Re_d dependence of instability to galloping, the critical galloping velocity U_{rc} and the $\hat{y}_c^* - U_r$ plots. Although not as strong, Reynolds number effects are also observed for sharp-corner cylinders, contradicting the common assumption of negligible Reynolds-number influence (which is mostly based on $Re_d > 10000$ range). In the presence of such Re_d dependence, the study demonstrates that meaningful comparison of FIV behavior across different studies should be done at the same ratio of the quasi-steady critical galloping reduced velocity $(U_{rc})_q$ to the vortex shedding reduced velocity U_{rs}, instead of the same Scruton number as usually done. Interestingly, unlike the known sharp-corner cylinder behavior, the round-corner cylinder exhibits no vortex-induced vibration-galloping interference even for $(U_{rs})_q/U_{rs} < 1$.

INTRODUCTION

While this study focuses on flow-induced vibration (FIV) of large-aspect-ratio rectangular cylinders, it serves as a surrogate for a broader class of FIV problems. We consider transverse y oscillation excited by vortex induced vibration (VIV), galloping and their mutual interaction (see Figure 1 for coordinates, flow and geometrical parameter definitions). These vibrations are typically characterized by suspending a *freely oscillating* cylinder in a flow facility and obtaining a plot of the oscillation amplitude $\hat{y}_c^* = \hat{y}_c/d$ versus the reduced velocity $U_r = U_\infty/fd$ (f is the oscillation frequency), as exemplified in Figure 2, by changing U_∞. This inevitably also produces variation in Reynolds number $Re_d = U_\infty d/\nu$ (ν is the kinematic viscosity), making it impossible to separate Re_d influences from those of U_r (i.e. the oscillation time scale). This ambiguity is not of concern when the Re_d effect is not important. While this is the general view in the case of a rectangular cylinder with sharp corners, geometrical modifications, such as rounding the corners of the cylinder, could lead to pronounced Re_d effects due to possible variation of the boundary layer separation location with Re_d. Moreover, even in the case of a sharp-corner cylinder, we showed that Re_d effects exist when $Re_d < 10{,}000$ (Naguib et al., 2024 and 2026).

The ambiguity can be resolved by taking advantage of *energy map* (EM) analysis. EMs are obtained from *forced oscillation* of a body over a wide range of $\hat{y}_c^*$ and U_r and the resulting energy (work) transfer between the flow and the body is computed from simultaneous force measurements. A powerful feature of EMs is that they can be used to predict the *free oscillation* amplitude of the body for a desired choice of the oscillator's mass, damping and stiffness (Menon and Mittal, 2019). Hence, by obtaining the EM at a fixed Re_d, characterization similar to Figure 2 can be obtained to reveal $\hat{y}_c^* - U_r$ behaviour *independent* of Re_d.The goal of the present study is to obtain EMs for a rectangular cylinder with *sharp* and *fully round* corners over the range $800 \leq Re_d \leq 9500$ where substantial Re_d influence on galloping instability is found. The maps will also be used to obtain and analyse the $\hat{y}_c^* - U_r$ behaviour at different Re_d values.

EXPERIMENTAL SETUP

Measurements are conducted in a closed-return water tunnel that has a 0.61×0.61 m test section. The test model cross-section geometry is as shown in Figure 1 for the round-corner cylinder with $d = 34$ mm, side ratio $c/d = 2$, and aspect ratio (span/thickness) $b/d = 15$. The cylinder is connected to rotational and linear servo motors via a six-component ATI Mini40 load cell. The rotary motor is used to control the cylinder's angle of attack (AoA) α, while the linear motor is employed to oscillate the cylinder in y direction at different frequencies and amplitudes. The rotary motor is only employed for measurement of the transverse force coefficient $C_y = F_y/(0.5\rho U_\infty^2 db)$ variation with AoA for the *static* cylinder. During y oscillation, the output of the load cell is measured simultaneously with the cylinder position y_c. The measured y_c is used as reference to obtain the phase-averaged force coefficient $\tilde{C}_y$ using 128 phase bins per cycle. Measurement uncertainties and detailed description of the setup may be found in Naguib et al. (2026).

DATA ANALYSIS

The non-dimensional mechanical work $W^* = W/(0.5\rho U_\infty^2 d^2 b)$ per oscillation cycle is calculated using

$$W^* = \int_0^{2\pi} \tilde{C}_y \dot{y}_c^* \mathrm{d}\theta = \pi \hat{\tilde{C}}_{y_o} \hat{y}_c^* \sin(\phi_o) \qquad (1)$$

where, $\dot{y}_c^* = \dot{y}_c/\omega_o d$ is the non-dimensional cylinder velocity, θ the oscillation cycle phase, $\hat{\tilde{C}}_{y_o}$ the phase-averaged transverse force coefficient amplitude at the oscillation frequency $\omega_o = 2\pi f_o$, and ϕ_o the phase angle by which the force leads the cylinder displacement at f_o. More details may be found in Naguib et al. (2026).

RESULTS

Galloping Instability - Re_d Effect

The instability of the cylinder to galloping is determined by the slope $\bar{C}_y - \alpha$ curve (where bar indicates a time average) of the *static* cylinder at zero AoA (e.g. Blevins, 2001). If this instability parameter a_g is positive, the cylinder is prone to galloping provided the reduced velocity exceeds a critical value U_{rc}. Figures 3(a) and 4(a) show $\bar{C}_y - \alpha$ results over the Re_d range investigated for the sharp- and round-corner cylinder respectively. Of particular importance is the behaviour of a_g, which for the sharp-corner cylinder exhibits an initial increase with Re_d up to $Re_d = 2500$, followed by a decrease at higher Reynolds numbers. Interestingly, for $Re_d \geq 5000$ (Figure 3b), no Reynolds number dependence is observed. This demonstrates that even the sharp-corner cylinder can exhibit Re_d effects when the Reynolds number is sufficiently low.

For the round-corner cylinder the influence of Re_d on a_g is more striking, with a_g switching from a negative value at the lowest Re_d (indicating stability to galloping) to a positive value over the range $Re_d = 1000 - 3200$ before reverting to a negative value with further Re_d increase. This behaviour is seen more clearly in Figure 4(b).

Energy Maps

The energy maps for the sharp- and round-corner cylinders are shown in Figures 5 and 6, respectively. The reduced velocity is normalized by the shedding reduced velocity, and the oscillation amplitude is expressed in terms of the apparent angle-of-attack amplitude $\hat{\alpha}$ instead of the nondimensional displacement amplitude $\hat{y}_c^*$. The two quantities are related through $\hat{\alpha} = \arctan(2\pi\hat{y}_c^*/U_r)$. For the sharp-corner cylinder, both Reynolds numbers yield qualitatively similar energy maps, with positive energy transfer to the cylinder (red shades) concentrated in two distinct regions. The first is a narrow yet tall region centered around $U_r/U_{rs} \approx 0.4$, and hence does not correspond to conventional VIV; this region is examined further in the following section. The second region occurs for approximately $U_r/U_{rs} > 1$ and remains unbounded with further increase in U_r. This region corresponds to the galloping mode of FIV. Together, these regions represent all feasible combinations of oscillation amplitude and reduced velocity that a freely oscillating cylinder may attain due to flow-induced excitation. Prediction of a specific oscillation amplitude and frequency from the energy map requires specification of the oscillator's mass, damping, and stiffness.

For the round-corner cylinder, a narrow region of positive energy transfer appears at $U_r/U_{rs} \approx 1$ for all three Reynolds numbers in Figure 6. Therefore, this region does correspond to VIV due to vortex shedding in the cylinder wake. As Re_d increases from 2500 to 3350, this VIV zone changes very little. By contrast, the unbounded galloping region observed at $Re_d = 2500$ shrinks markedly at $Re_d = 3200$ and disappears altogether at $Re_d = 3350$. This trend is consistent with the decrease in a_g and its subsequent sign change to negative with increasing Re_d over this range.

Amplitude – Reduced Velocity Plots

To produce $\hat{y}_c^* - U_r$ plots similar to Figure 2 using the EMs, the mechanical parameters of the oscillator are specified, and the damping work W_d^* is equated to W^*, where

$$W_d^* = 4\pi^2 Sc(\,\hat{y}_c^{*2}/U_r^2)\,(c/d) \qquad (2)$$

with Sc being the Scruton number, or the mass-damping parameter, of the oscillator

$$Sc = 4\pi(m/\rho dcb)\zeta = 4\pi m^* \zeta \qquad (3)$$

where, m is the cylinder mass, m^* the mass ratio, and ζ the damping ratio. Equating (1) and (2)

$$4\pi^2 Sc(\,\hat{y}_c^{*2}/U_r^2)\,(c/d) = W^*(\,\hat{y}_c^*, U_r) \qquad (4)$$

In Equation (4), U_r is specified (in practice this is set by the natural frequency of the oscillator, which depends on the oscillator's mass and stiffness), and one can solve for the only remaining unknown, $\hat{y}_c^*$. Hence by varying U_r over the range of interest, the $\hat{y}_c^* - U_r$ plot is obtained. Equation (4) may produce multiple $\hat{y}_c^*$ solutions, but only those corresponding to $\partial W^*/\partial \hat{y}_c^* < 0$ are stable, and hence feasible in practice (Morse and Williamson, 2009).

Following the above procedure, the $\hat{y}_c^* - U_r$ plots for the sharp-corner cylinder are obtained using the energy maps in Figure 5 and compared with the results of Washizu et al. (1978) at the same Sc values. The comparison, shown in Figure 7, presents U_r normalized by the vortex-shedding reduced velocity U_{rs}. Focusing on the lowest Sc value, the present results agree well qualitatively with those of Washizu et al. Both studies exhibit a narrow range of amplitude-limited oscillations near $U_r/U_{rs} \approx 0.4$, which lies well below the lock-in range associated with wake-induced VIV. Naudascher and Rockwell (1993) attributed this response in Washizu et al.'s data to oscillations driven by impinging leading-edge vortices (ILEV), rather than conventional VIV. Similar behavior was observed by Mannini et al. (2016), albeit for a cylinder with $c/d = 1.5$. The close correspondence in the U_r/U_{rs} range of these ILEV-induced oscillations between the present results and those of Washizu et al., despite the difference in Reynolds number and the way the data are obtained, is remarkable.

The unbounded increase of $\hat{y}_c^*$ with U_r, characteristic of galloping, is evident in both the present results and those of Washizu et al. at $Sc = 3$. However, the critical reduced velocity for the onset of galloping U_{rc} exhibits a clear dependence on Reynolds number. Specifically, Washizu's higher-Re_d data show U_{rc} slightly below U_{rs}, whereas the present results at $Re_d = 7500$ yield $U_{rc} \approx U_{rs}$, and those at $Re_d = 2500$ exhibit U_{rc} exceeding U_{rs}. Noting that the data of Washizu et al. do not correspond to a fixed Reynolds number, the results in Figure 7 nonetheless suggest a systematic trend in which U_{rc} increases with decreasing Reynolds number.

As Sc increases to 40, the ILEV-driven oscillations are eliminated in both studies, leaving only a galloping range of oscillation. At an even higher Scruton number ($Sc = 50$), however, the two investigations exhibit markedly different qualitative behavior. In Washizu et al.'s data, a VIV region emerges in the vicinity of $U_r/U_{rs} = 1$, accompanied by a shift of the galloping critical velocity to a value significantly larger than the slightly below-U_{rs} values observed at lower Sc. By contrast, the present results do not exhibit VIV behavior, and the critical velocity for galloping is not significantly different from that at lower Sc values. We attribute this stark difference between the two studies to the fact that comparisons at the same Scruton number are only meaningful when Reynolds number effects are negligible. This point is clarified below.

Mannini et al. (2016) showed that the appearance of distinct VIV and galloping regions (as observed in Washizu et al.'s data at $Sc = 50$) depends on the ratio $(U_{rc})_q/U_{rs}$, where $(U_{rc})_q$ is the quasi-steady critical galloping velocity, given by

$$(U_{rc})_q/U_{rs} = (2Sc/a_g U_{rs})(c/d) \tag{5}$$

The values of U_{rs} and a_g for the present study and for Washizu et al. are listed in Table 1, and the corresponding $(U_{rc})_q/U_{rs}$ values are indicated in Figure 7. A significant variation in $(U_{rc})_q/U_{rs}$ is observed among the different cases. Since the U_{rs} values differ by less than 10%, the substantial variation in $(U_{rc})_q/U_{rs}$ is attributed primarily to differences in a_g, which exhibits a visible dependence on Re_d, consistent with the $\bar{C}_y - \alpha$ behavior shown in Figure 3(a).

Table 1. Values of reduced velocity of shedding and galloping instability parameter for different cases.

Geometry/Study	Re_d	U_{rs}	a_g
Sharp	2500	11.4	15.4
Sharp	7500	13.5	9.6
Round	2500	4.2	5.6
Round	3200	4.1	2.4
Round	3350	4.0	-0.4
Washizu et al.	$0.2 - 3.3 \times 10^5$	12.6	4.7

Moreover, the largest $(U_{rc})_q/U_{rs}$ value for the present data in Figure 7 is 1.53, which falls within the regime identified by Mannini et al. as full interference between VIV and galloping ($(U_{rc})_q/U_{rs} < 2.15$). This regime is characterized by the absence of a distinct VIV region and $U_{rc} \approx U_{rs}$. In contrast, Washizu et al.'s data at $Sc = 50$ yield $(U_{rc})_q/U_{rs} = 3.37$, placing it well within the *no-interference* regime of Mannini et al., which is associated with distinct VIV (provided that VIV persists despite the increased Sc) and galloping regions, and $U_{rc} > U_{rs}$.

The above demonstrates that comparing different cases at the same Scruton number is meaningful only in the absence of Re_d effects. To account for such effects, the results in Figure 7 are compared in Figure 8 at the same $(U_{rc})_q/U_{rs}$ values. The corresponding Sc values are indicated on the plots. The ability to adjust Sc to match a prescribed $(U_{rc})_q/U_{rs}$ without physically modifying the oscillator in free-oscillation experiments highlights a key advantage of the EM-based approach.

Figure 8 shows that the case exhibiting a qualitative discrepancy in Figure 7 ($Sc = 50$) now appears more consistent between the present results and those of Washizu et al. Specifically, at $Re_d = 7500$, two distinct regions are observed: one near $U_r = U_{rs}$, spanning a limited range of U_r values and presumably corresponding to VIV, and another corresponding to galloping at U_{rc} values significantly greater than U_{rs}. In contrast, the lower $Re_d = 2500$ case does not exhibit a VIV region, although it does show a noticeable increase in U_{rc} above U_{rs}.

The absence of VIV at $Re_d = 2500$ in comparison to $Re_d = 7500$ in Figure 8(c) is believed to be due to the increased damping associated with the higher Scruton number at $Re_d = 2500$. Additionally, the strength and organization of vortex shedding, which depend on Re_d, likely play a role and may be also connected to the "data scatter" seen in the VIV region at $Re_d = 7500$ in comparison to Washizu et al.'s data. Also noteworthy is that the sudden jump in $\hat{y}_c^*$ at U_{rc} observed in the present data in Figure 8(c) is likewise evident in the data of Mannini et al. within the no-interference regime.

The $\hat{y}_c^*$–U_r/U_{rs} plots for the round-corner cylinder at $Sc = 3$, 40, and 50 are shown in Figure 9(a) for the same Re_d values as the EMs in Figure 6. The ordinate scale is ten times larger than in Figures 7 and 8; therefore, to make the VIV range visible, a second plot focusing on this range is provided in Figure 9(b). For this geometry, there are no published data for direct comparison. Although difficult to discern in Figure 9(b), the VIV region appears only at the lowest Scruton number and shows virtually no change over the narrow Reynolds-number range of the data. In contrast, the galloping oscillations exhibit a pronounced Reynolds-number dependence over the same range: the oscillations are strongest at $Re_d = 2500$ and are absent at $Re_d = 3350$. Another notable trend is the increase in U_{rc} as Re_d rises from 2500 to 3200. Both Reynolds-number trends are consistent with the previously observed a_g dependence on Reynolds number (see Figure 1). Crucially, these behaviors would not be captured by the traditional approach of generating $\hat{y}_c^*$–U_r plots through systematic increase in U_∞ to vary U_r. Finally, we note that for $Re_d = 2500$ and $Sc = 3$, $(U_{rc})_q/U_{rs} = 0.51$; nevertheless, the data do not show the full interference between VIV and galloping reported for sharp-corner cylinders in the literature and observed in the present sharp-corner results. This intriguing outcome suggests that cylinder-corner rounding may alter the interference mechanism and warrants a dedicated future study.

CONCLUSIONS

This work highlights the potentially significant effects of Reynolds number $\boldsymbol{Re_d}$ on the flow-induced vibration (FIV) of large-aspect-ratio rectangular cylinders. These effects are typically masked by the traditional experimental approach used to characterize the vibration-amplitude $\hat{\boldsymbol{y}}_c^*$ variation with reduced velocity $\boldsymbol{U_r}$ employing a freely oscillating cylinder. The results demonstrate that energy maps provide an effective means to remove Reynolds-number influence from $\hat{\boldsymbol{y}}_c^*$–$\boldsymbol{U_r}$ plots, thereby isolating $\boldsymbol{U_r}$ effects from those associated with $\boldsymbol{Re_d}$ and enabling deeper physical insight into FIV phenomena. This approach is applied to the study of FIV of sharp- and round-corner rectangular cylinders over the range $\boldsymbol{Re_d = 800–9500}$.

Galloping behavior of the round-corner cylinder is found to exhibit high sensitivity to $\boldsymbol{Re_d}$ over a narrow range, $\boldsymbol{Re_d \approx 800–3350}$. Specifically, the cylinder is stable to galloping at the lower end of this range, becomes unstable near $\boldsymbol{Re_d \approx 1000}$, and reverts to stability at $\boldsymbol{Re_d \approx 3350}$ and higher Reynolds numbers. Inspection of the energy maps at $\boldsymbol{Re_d = 2500}$, $\boldsymbol{3200}$, and $\boldsymbol{3350}$ show significant Reynolds number effect on the critical velocity of galloping $\boldsymbol{U_{rc}}$ and the amplitude-reduced velocity plots of $\boldsymbol{Re_d = 2500}$ and $\boldsymbol{3200}$. By contrast, VIV behavior showed no $\boldsymbol{Re_d}$ influence among all three Reynolds numbers. Intriguingly, distinct VIV and galloping response regions are observed in the amplitude–reduced-velocity plots even when the quasi-steady critical reduced velocity of galloping $\boldsymbol{(U_{rc})_q}$ is less than the vortex shedding reduced velocity $\boldsymbol{U_{rs}}$. This suggests that the VIV–galloping interference mechanism, well documented for sharp-corner cylinders, may not be present for round-corner geometries.

Although weaker than for round-corner cylinders, $\boldsymbol{Re_d}$ effects are also evident for sharp-corner cylinders, contradicting the common assumption that Reynolds-number influence is negligible—an assumption largely based on studies conducted at $\boldsymbol{Re_d > 10000}$. When such $\boldsymbol{Re_d}$ dependence is present, meaningful comparison of FIV behavior across different studies should be performed at the same $\boldsymbol{(U_{rc})_q/U_{rs}}$, rather than at the same Scruton number, as is conventionally done.

ACKNOWLEDGEMENT

This work is supported by U.S. Army CCDC Soldier Systems Center grant number W911QY2410001, monitored by Dr. Keith Bergeron. The views and conclusions contained in this document are those of the authors and should not be interpreted as representing the official policies, either expressed or implied, of the U.S. Army CCDC Soldier Systems Center or the U.S. Government.

REFERENCES

Blevins, R. D., 2001, “Flow-Induced Vibration,” Second Ed., Krieger Publishing Company, Malabar, FL.

Menon, K., and Mitall, R., 2019, “Flow Physics and Dynamics of Flow-Induced Pitch Oscillations of an Airfoil”, *Journal of Fluid Mechanics*, Vol. 877, pp. 582-613.

Mannini, C., Marra, A. M., Massai, T., and Bartoli, G., 2016, “Interference of Vortex-Induced Vibration and Transverse Galloping for a Rectangular Cylinder,” *Journal of Fluids and Structures*, Vol. 66, pp 403-423.

Morse, T. L., and Williamson, C. H. K., 2009, “Prediction of Vortex-Induced Vibration Response by Employing Controlled Motion”, *Journal of Fluid Mechanics*, Vol. 634, pp. 5-39.

Naguib, A. M., Ferro, M. A., Safaripour, A., and Koochesfahani, M. M., 2024, “On Quasi-Steadiness of Transverse Galloping of Rectangular Cylinders at Reynolds Numbers Below 10,000,” *Journal of Fluids and Structures*, Vo. 125, 20 pp.

Naguib, A. M., Cruikshank, R., Safaripour, A., Olson, D. A., and Koochesfahani, M. M., 2026, “Reynolds Number and Geometry Effects on Quasi-Steadiness of Heaving Rectangular Cylinders,” *AIAA Journal*, Vol. 64 (1), pp. 116-126.

Naudascher, E., and Rockwell, D., 1993, “Flow-Induced Vibrations – An Engineering Guide,” CRC Press, pp. 308-310.

Washizu, K., Ohya, A., Ostsuki, Y., and Fuji, K., 1978, “Aeroelastic Instability of Rectangular Cylinders in a Heaving Mode,” *Journal of Sound and Vibration*, Vol. 59 (2), pp. 195-210.

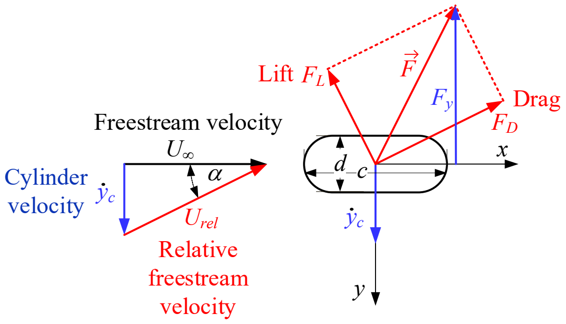

Figure 1. Flow configuration for the round-corner cylinder. α is the apparent AoA during cylinder oscillation and F_y is the transverse aerodynamic force.

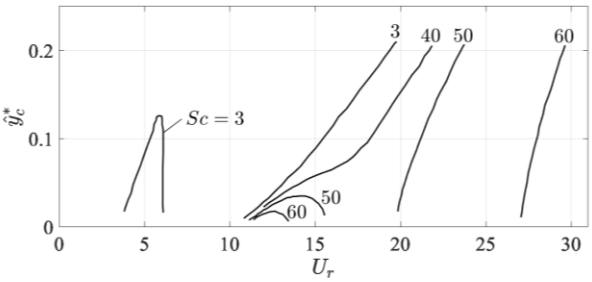

Figure 2. Amplitude-reduced velocity plots of freely oscillating sharp-corner rectangular cylinder over the range $2 \times 10^4 < Re_d < 3.3 \times 10^5$ (reproduced from Washizu et al., 1978).

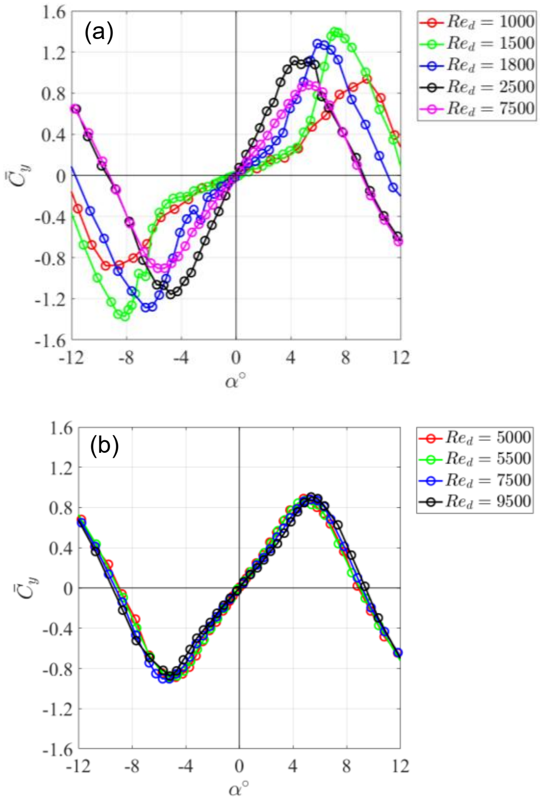

Figure 3. Mean transverse load characteristics for the static sharp-corner cylinder: cases representative of (a) the full Re_d range, and (b) $Re_d \geq 5000$.

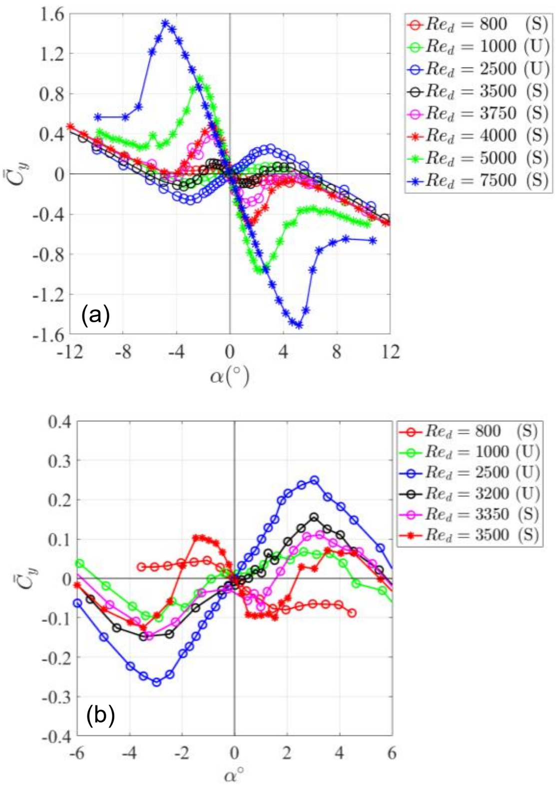

Figure 4. Mean transverse force characteristics for the static round-corner cylinder: cases representative of (a) the full Re_d range, and (b) the vicinity of a_g sign switch. S and U in the legend indicate stability and instability to galloping respectively.

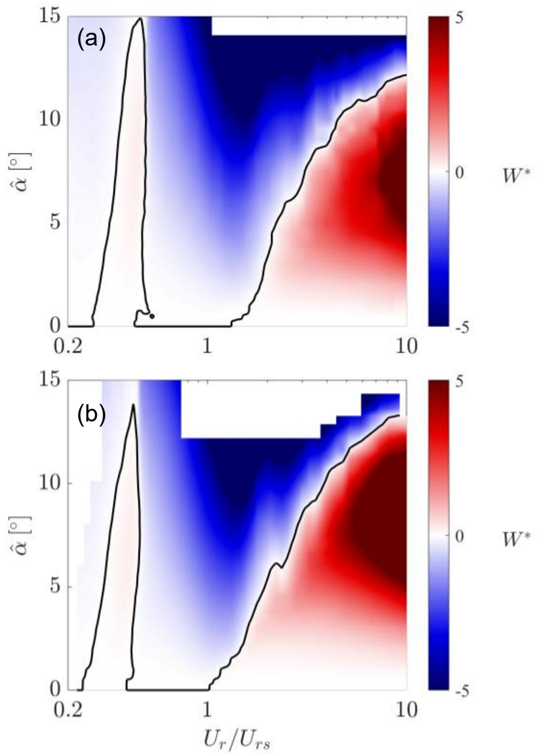

Figure 5. Energy map for the sharp-corner cylinder: (a) $Re_d = 2500$, and (b) $Re_d = 7500$.

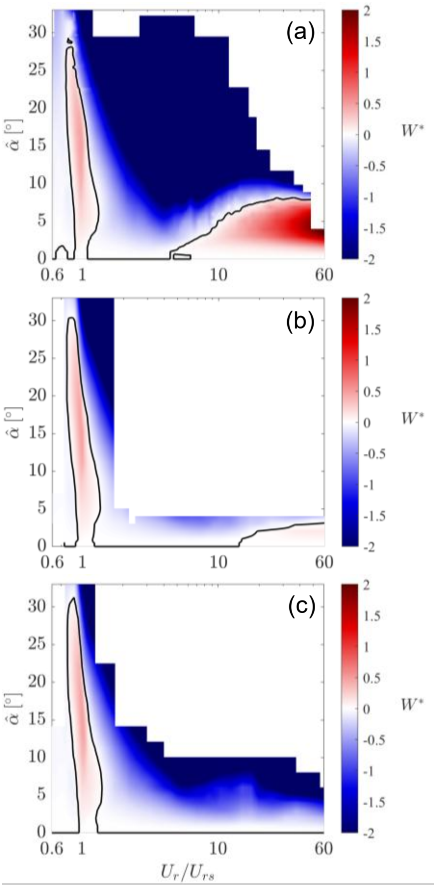

Figure 6. Energy map for the round-corner cylinder: (a) $Re_d = 2500$, (b) $Re_d = 3200$, and (c) $Re_d = 3350$.

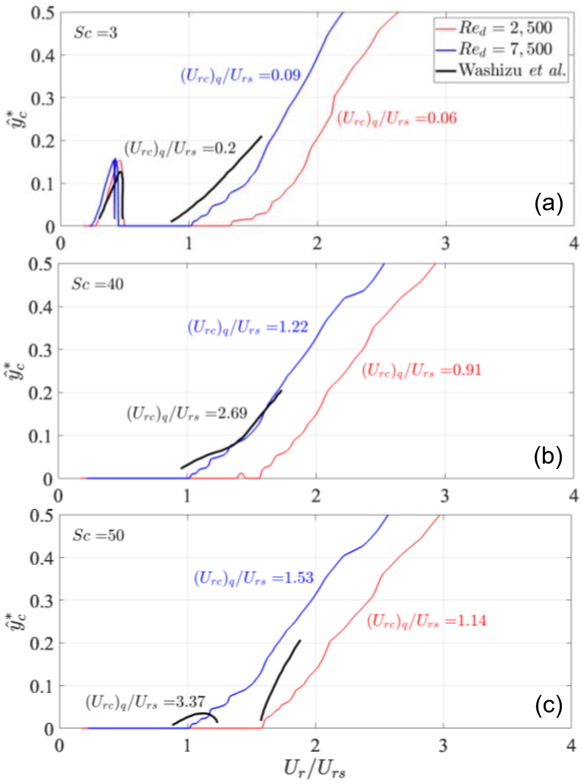

Figure 7. Amplitude-reduced velocity characteristics of the sharp-corner cylinder compared to Washizu et al. (1978) data at Scruton number of (a) $Sc = 3$, (b) $Sc = 40$, (c) $Sc = 50$.

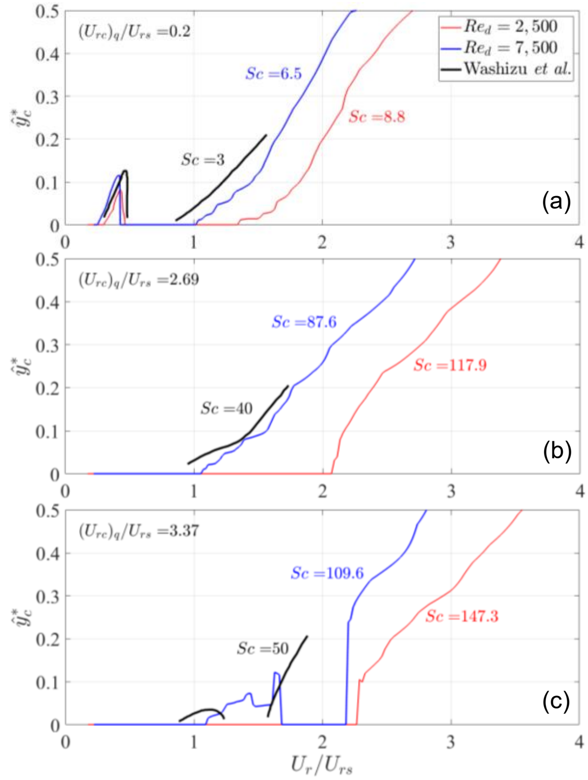

Figure 8. Amplitude-reduced velocity characteristics of the sharp-corner cylinder compared to Washizu et al. (1978) data at U_{rc}/U_{rs} value of (a) 0.2, (b) 2.69, (c) 3.37.

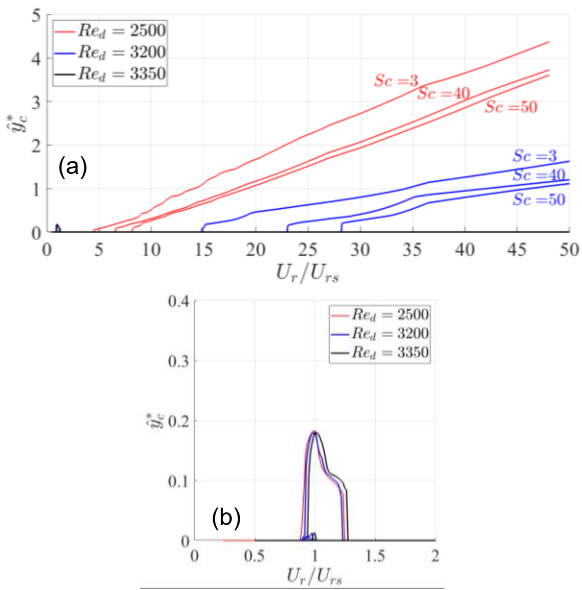

Figure 9. (a) Amplitude-reduced velocity characteristics of the round-corner cylinder for different Reynolds and Scruton numbers. (b) Magnification of the VIV range near $U_r = U_{rs}$.